

# Weak mantle wedge causes mantle exhumation punctuated with discrete oceanic crust in the Tyrrhenian basin

Received: 9 March 2025

Hao Su<sup>1,2</sup>, Wei Leng<sup>1,3</sup> , Jie Liao <sup>2,4</sup>  & Sascha Brune<sup>5,6</sup>

Accepted: 16 December 2025

Published online: 13 January 2026

 Check for updates

The Continent-Ocean Transition (COT) in the young Tyrrhenian basin documents mantle exhumation punctuated with multiple episodes of discrete oceanic crust formation. This observation challenges prevailing models of magma-poor COTs, which typically describe mantle exhumation preceding the emplacement of oceanic crust. Notably, this COT developed without the conventional conditions associated with magma-poor rifted margins, such as slow rifting velocities and chemically depleted mantle sources. A key observation is the low shear-wave velocity observed in the uppermost mantle of the Tyrrhenian basin and its adjacent onshore regions, which correlates with subduction-related volcanism, suggesting the presence of a hydrated mantle wedge with low rheological strength. Here, we show that, based on 3D magmatic-thermomechanical numerical modeling, the episodic formation of oceanic crust within the Tyrrhenian basin's COT results from the mechanical weakness of the mantle. The lithospheric mantle is exhumed to the surface through exhumation channels initiated within the weak mantle zone. The subsequent flow of partially molten mantle toward these channels leads to the development of multiple short-lived spreading centers. Our findings shed light on characteristics and mechanisms shaping the COT of marginal basins, where their opening is influenced by subduction processes.

The discovery of exposed mantle by drilling in the COT west of Iberia prompted the development of conceptual models for magma-poor rifted margins. These margins are characterized by minimal syn-rift magmatism and, in some cases, by a broad zone of exhumed mantle that shows little to no magmatism prior to the formation of mature oceanic crust<sup>1–5</sup>. However, limited by the scarce evidence obtained in ultra-deepwater drilling and low-resolution geophysics, the nature and genesis of the magma-poor COT is still controversial<sup>6–9</sup>. Two primary conditions have been proposed for the formation of magma-poor rifted margins: (1) Slow extension results in low upwelling rates, which in

turn enhance asthenospheric cooling and reduce melt production<sup>10,11</sup>; (2) Upwelling mantle with chemically depleted composition, too refractory to melt<sup>10,12</sup>.

The Tyrrhenian basin in the Mediterranean Sea was formed by extension of continental lithosphere above the retreating Ionian slab during the Neogene<sup>13,14</sup> (Fig. 1a). Facilitated by the shallow water and thin sediment cover, high-quality geological and geophysical data have been obtained and analyzed<sup>13–22</sup>. The Tyrrhenian basin therefore, constitutes an ideal natural laboratory for investigating the formation of the COT in magma-poor settings<sup>9</sup>. It has been proposed that the

<sup>1</sup>State Key Laboratory of Precision Geodesy, School of Earth and Space Sciences, University of Science and Technology of China, Hefei, China. <sup>2</sup>School of Earth Sciences and Engineering, Sun Yat-Sen University, and Southern Marine Science and Engineering Guangdong Laboratory (Zhuhai), Zhuhai, China. <sup>3</sup>Mengcheng National Geophysical Observatory, University of Science and Technology of China, Mengcheng, China. <sup>4</sup>Guangdong Provincial Key Lab of Geodynamics and Geohazards, Zhuhai, China. <sup>5</sup>GFZ Helmholtz Centre for Geosciences, Potsdam, Germany. <sup>6</sup>Institute of Geosciences, University of Potsdam, Potsdam-Golm, Germany.  e-mail: [wleng@ustc.edu.cn](mailto:wleng@ustc.edu.cn); [liaojie5@mail.sysu.edu.cn](mailto:liaojie5@mail.sysu.edu.cn)

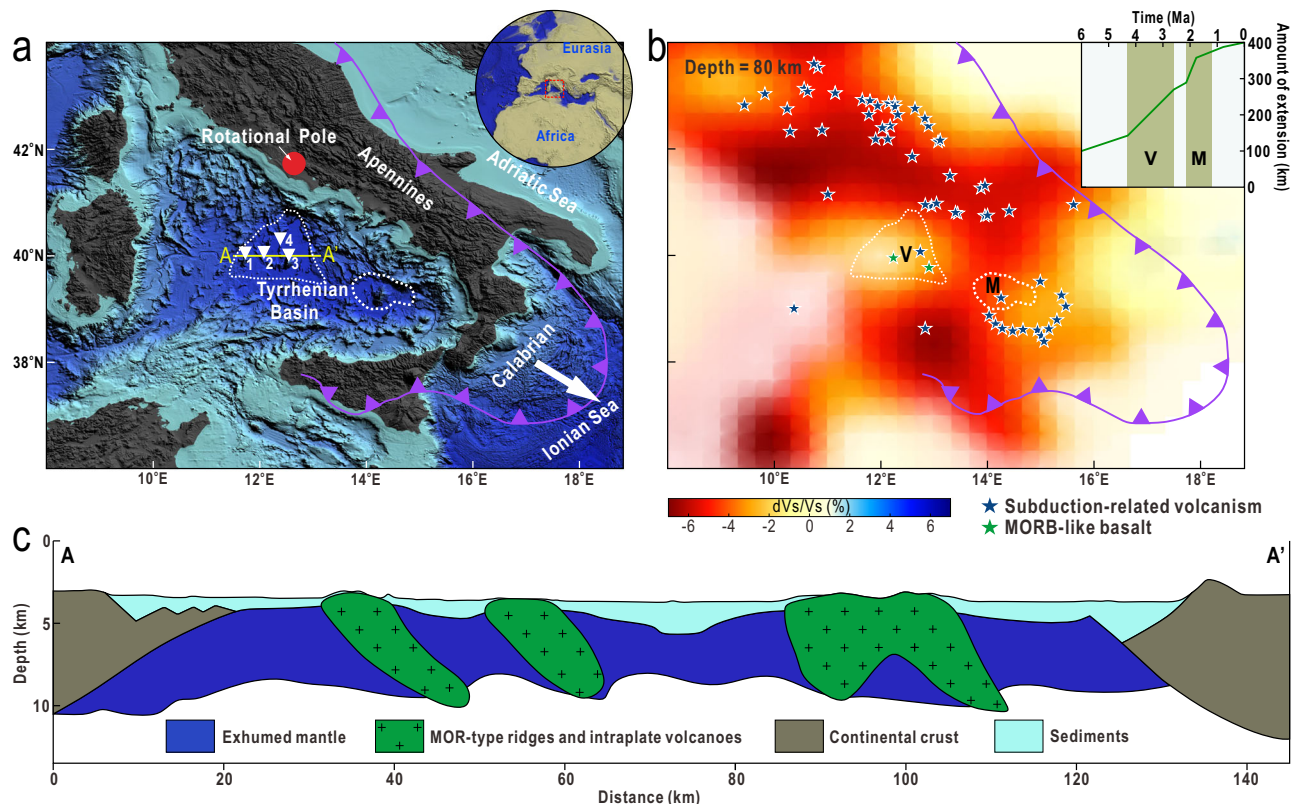


**Fig. 1 | Integrated geological records related to mantle exhumation, oceanic accretion, and hydrated mantle wedge in the Tyrrhenian basin.** **a** Tectonic sketch map of the Tyrrhenian basin and its surrounding areas<sup>18,20</sup>. The purple arrows show the subduction of the Ionian slab. The white arrow shows the extension direction. The red circle shows the location of rotational pole of Vavilov basin<sup>38</sup>. The white triangles show the magmatic seamounts inferred from dredging and drilling information, 1: Magnaghi volcano, 2: D'Ancona Ridge, 3: Vavilov

volcano, 4: Gortani Ridge<sup>20</sup>. **b** Subduction-related volcanism, MORB-like basalt and shear-wave velocity anomaly at a depth of 80 km<sup>18</sup>, the white dotted cycles show the outlines of Vavilov (V) Basin and Marsili (M) Basin. The inset shows the amount of extension in the Tyrrhenian Sea during the past 6 million years<sup>25</sup>. **c** Lithosphere structure along profiles AA' showing the basement of the Tyrrhenian basin consisting of extensive exhumed continental lithospheric mantle punctuated with multiple short-lived oceanic crust<sup>20</sup>.

basement of the Tyrrhenian basin is composed of extensive exhumed mantle<sup>14–21</sup> (Fig. 1c). This observation conflicts with current wisdom on magma-poor rifted margins, as mantle exhumation in the Tyrrhenian basin is punctuated with multiple discrete events of magmatic emplacement (~5–2 Ma)<sup>19,20</sup> (Fig. 1c).

The conventional two conditions to explain the formation of magma-poor margins (slow rifting or depleted mantle) can hardly be reconciled with the COT in the Tyrrhenian basin for the following reasons: (1) The full extension rate is about 4–6 cm/yr during the opening of the Vavilov and Marsili sub-basins of the Tyrrhenian basin<sup>23–25</sup> (Fig. 1b), which is about 3 to 5 times faster than the half extension velocities of <0.6 cm/yr required for magma-poor mantle exhumation at rifted margins<sup>10</sup>; (2) The peridotites sampled in the Tyrrhenian COT are heterogeneous and on average mineralogically fertile<sup>26</sup>. Magni et al.<sup>27</sup> suggested that episodic extension, driven by intermittent trench retreat, could explain the ridge jump from Vavilov Basin to Marsili Basin. However, within the Vavilov Basin, continuous opening is observed<sup>20,25</sup>. Why this continuous extensional regime produced mantle exhumation punctuated with multiple short-lived spreading centers (magmatic emplacement) remains unresolved.

The pronounced low shear-wave velocity anomaly in the uppermost mantle (~40–80 km) beneath the Tyrrhenian basin and onshore regions is well documented<sup>18,28,29</sup> (Fig. 1b). This anomaly spatially correlates with subduction-related volcanism (14–0 Ma) suggests the presence of a hydrated mantle wedge formed by present or past slab dehydration<sup>18</sup> (Fig. 1b). Also, the magmatic products (Mid Ocean Ridge type basalts and alkaline lavas) observed in the Tyrrhenian basin

suggest the presence of fluids released from the dehydration of the subducted plate<sup>20</sup>. Hydrated mantle is likely characterized by low rheological strength<sup>29,30</sup>. A weak crust has been recognized for promoting depth-dependent extension and strain migration during continental rifting<sup>31–37</sup>. In line with this concept, we hypothesize that a weak mantle wedge may exert a similar influence, potentially facilitating mantle exhumation and the migration of spreading centers in the Tyrrhenian Basin.

In this work, we conduct 3-D magmatic-thermomechanical numerical models tailored to the Tyrrhenian Basin's geology. Our simulations demonstrate how a weakened mantle wedge can trigger mantle exhumation punctuated with multiple discrete oceanic crust. Systematic parameter sensitivity studies further identify key controls governing these geodynamic processes.

## Results

### Mantle exhumation punctuated by multiple discrete oceanic crust

We conducted numerical models to explore the effects of a weak mantle zone on mantle exhumation and magmatism during continental rifting. The initial model configuration (Supplementary Fig. 1), rock rheologies, and material properties are described in the Methods and the Supplementary Table 1. In our models, the weak mantle (water-saturated) zone with a low friction coefficient is positioned in the northeastern part ( $x = 292$ –584 km). In contrast, the southwestern model domain ( $x = 0$ –292 km) retains intact mantle rheology (Supplementary Fig. 1). This geological contrast enables us to examine how

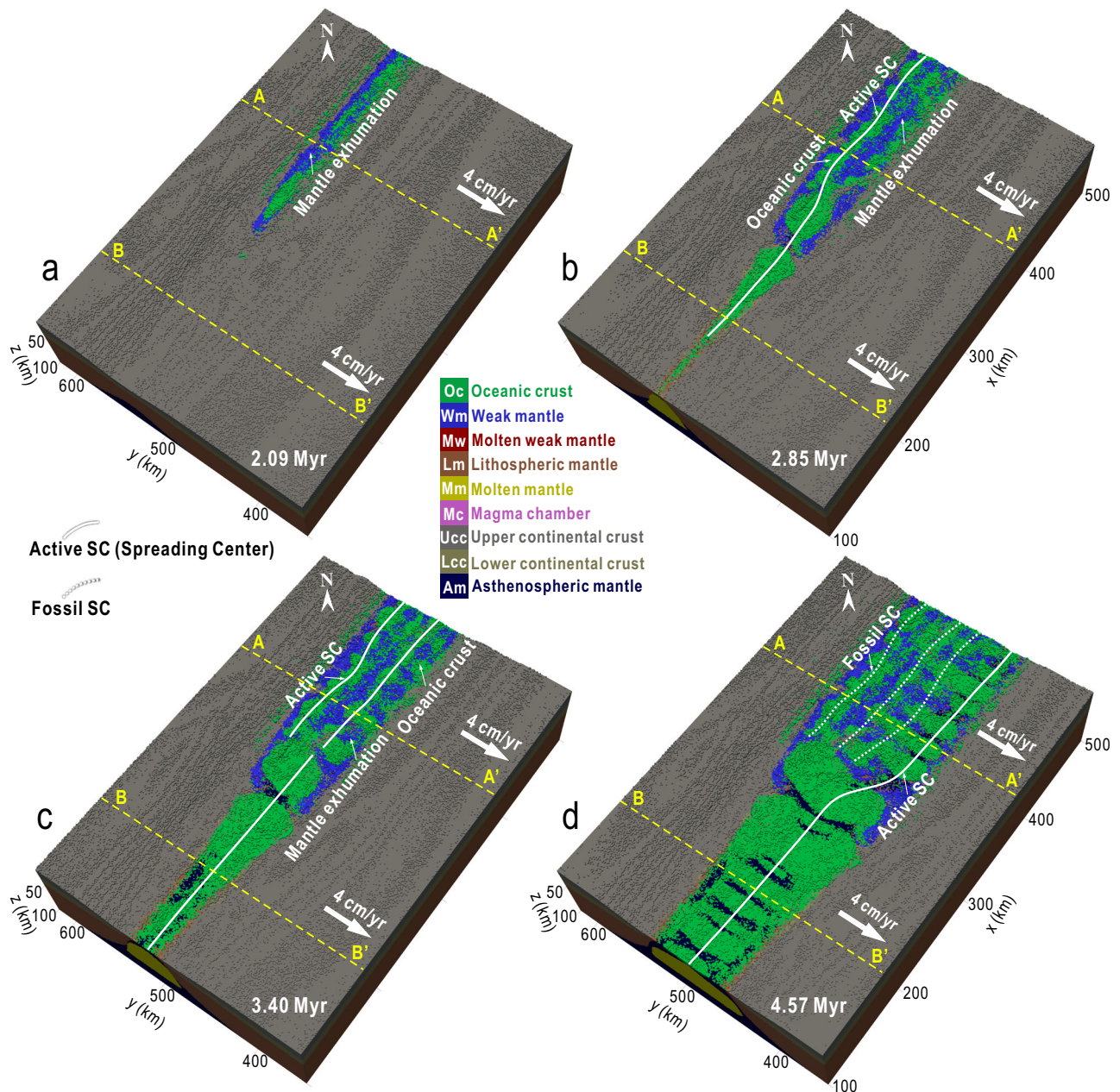


**Fig. 2 | Model results of mantle exhumation punctuated with discrete oceanic crust emplacement.** **a–d** Model snapshots of composition shown at  $t = 2.09$  Myr, 2.85 Myr, 3.40 Myr and 4.57 Myr, respectively. The white solid/dotted lines are the position of the active/fossil spreading center, the yellow dashed line marks the positions of the cross sections shown in Fig. 3 (A–A') and supplementary Fig. 2 (B–B').

These graphs clearly show that lithospheric mantle exhumation is punctuated by discrete oceanic crust emplacement in the northeastern domain (with a weak mantle zone), and symmetric continental rifting followed by stable oceanic spreading in the southwestern domain (without a weak mantle zone).

lateral variations in rheological properties affect the style of rifting and continental break-up. To simulate the trench retreat process, a high extension rate of 4 cm/yr is imposed on the southeastern boundary ( $y = 0$ ), consistent with the southeastward trench retreat velocity during the opening of the Vavilov and Marsili sub-basins<sup>23,25</sup> (Fig. 1b).

Figures 2 and 3 illustrate the process of how a weak mantle zone induces lithospheric mantle exhumation punctuated with multiple discrete oceanic crust, in the reference model (mf3). This weak mantle zone is defined by a low friction coefficient ( $\mu = 0.001$ ), spanning 40 km laterally ( $y = 560\text{--}600$  km) and vertically ( $z = 60\text{--}100$  km). In this model, crustal break-up occurs at 2.09 million years (Myr), whereby lithosphere thinning and asthenosphere upwelling are

focused above the weak mantle zone (Figs. 2a, 3a). During this process, two exhumation channels with highest extensional strain rate emerge within the weak mantle zone beneath the southeast and northwest continental margins (Fig. 3b). The lithospheric mantle is exhumed to the surface along the exhumation channels (Figs. 2a, 3a). As the extension continues, a spreading center is firstly formed with oceanic crust emplacement atop the partially molten mantle (Figs. 2b; 3c). This marks the formation of mantle exhumation punctuated with magmatic emplacement. The exhumation channel beneath the southeastern margin continues to be active, exhibiting peak extensional strain rates in this region. This rapid extension facilitates the inflow of low-density, low-viscosity, partially molten mantle material toward the channel,

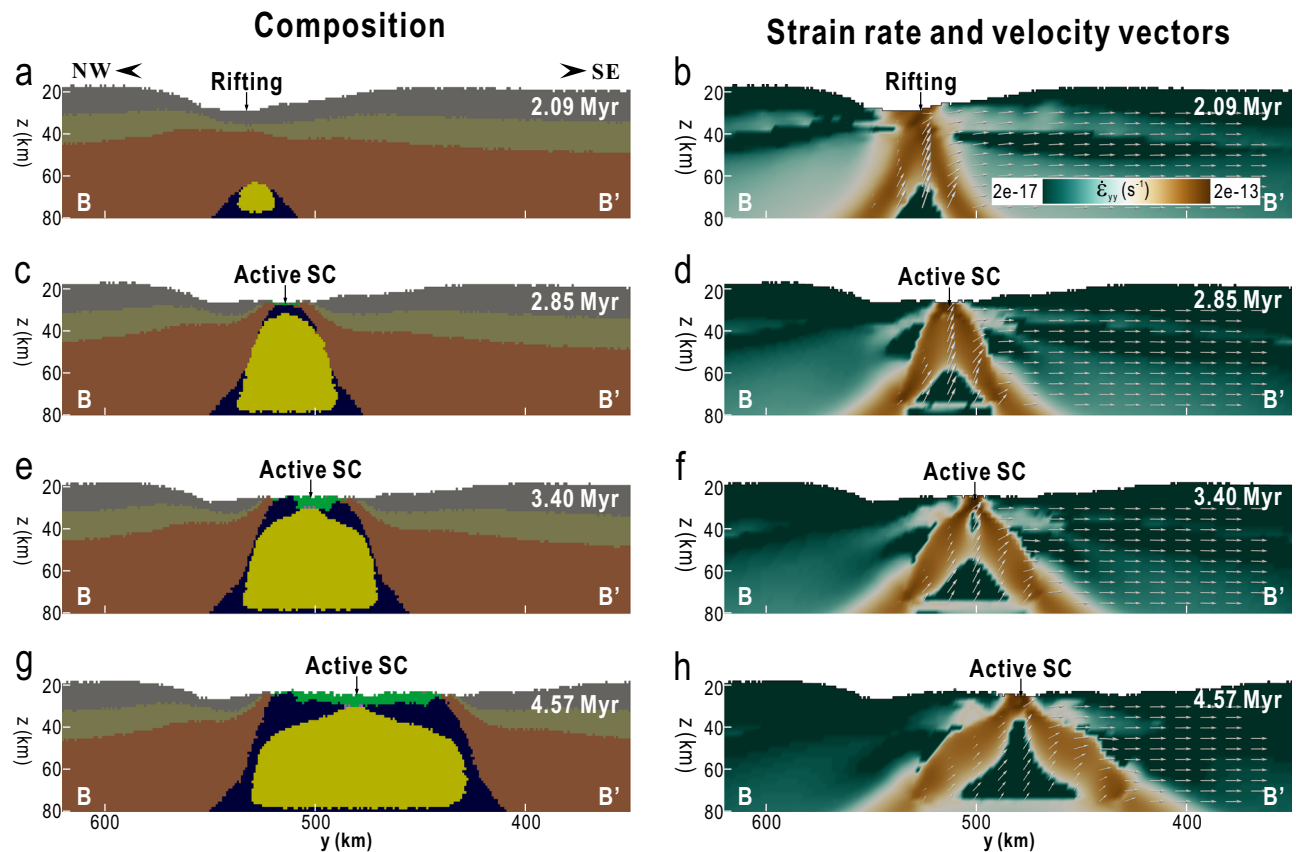


**Fig. 3 | Weak mantle wedge causes mantle exhumation punctuated with discrete oceanic crust.** Left column (a, c, e, g): Compositional field profiles, the colors are the same as in Fig. 2, the numbers 1, 2, and 3 denote the sequence of magmatic emplacement events. Right column (b, d, f, h): Vertical cross-sections of extensional strain rate and velocity field (depicted as arrows). White dashed lines

represent the exhumation channels. These graphs show that lithospheric mantle is exhumed to the surface through exhumation channels initiated within the weak mantle zone. The flow of partially molten mantle towards these channels leads to the development of multiple short-lived spreading centers.

where it fills the newly formed space (Fig. 3d). By 3.40 Myr, a larger volume of the lithospheric mantle is exposed (Figs. 2c, 3e). Concurrently, as the partially molten mantle consistently flows toward the exhumation channel, the model successively forms new spreading centers (atop of the molten mantle) toward the southeast, with oceanic crust being emplaced independently above each spreading center (Fig. 3e, f). Eventually, at 4.57 Myr, as the weak mantle beneath the southern margin diminishes, the exhumation channel ceases activity. The molten mantle gathers below the new spreading center and the system transitions to a steady-state configuration (Figs. 2d, 3g, h). The youngest spreading center remains active, while the old spreading centers become abandoned as the partially molten mantle flows to the newly established spreading center (Figs. 2d, 3g, h). Our models therefore suggest that mantle exhumation punctuated with multiple discrete oceanic crust emplacements is triggered by the weak mantle zone.

As a comparison, in the southwestern part of the model ( $x=0-292$  km) where there is no weak lithospheric mantle, the extensional deformation is rather symmetric. As the lithosphere thins, the continental crust is coupled with the lithospheric mantle and breaks apart simultaneously (Fig. 2a, b; Supplementary Figs. 2a–f), leading to symmetric rifted margins and negligible exposure of the continental lithospheric mantle. During the spreading phase, the strain is always localized at the mid-ocean ridge (Fig. 2c, d; Supplementary Figs. 2g–l). The oceanic crust on both sides of the ridge is symmetrically accreted, and only one spreading center developed during the simulation.

### Effect of varying weak mantle friction coefficient, thickness, width, and extension velocity

To investigate the conditions governing mantle exhumation punctuated by discrete oceanic crust emplacement, we systematically vary key parameters of the weak mantle zone across numerical models. These parameters include: friction coefficient (mf series: mf1–mf4), lateral width (mw series: 20–50 km), vertical thickness (mt series: 20–50 km), and extension velocity (mv3), with detailed specifications provided in Supplementary Table 2. In model mf1 (weak mantle friction coefficient = 0.1), short-lived exhumation channels develop within the weak mantle zone. This configuration produces symmetric rifted margins with minimal lithospheric mantle exposure (Fig. 4a; Supplementary Fig. 3a). Model mf2 (weak mantle friction coefficient = 0.01) develops exhumation channels within the weak mantle zone, and lithospheric mantle is exposed along the exhumation channel beneath the southeastern margin, accompanied by southeastward migration of the spreading center (Fig. 4a; Supplementary Fig. 3b). The end-member model mf4 (weak mantle friction coefficient = 0), exhibits a long-lived exhumation channel activity. This prolonged tectonic regime results in extensive lithospheric mantle exposure at the surface and facilitates multiple discrete oceanic crust emplacement events (Fig. 4a; Supplementary Fig. 3c).

Model mw20 (weak mantle width = 20 km) fails to develop exhumation channels, resulting in minimal lithospheric mantle exposure and a single spreading center (Fig. 4b; Supplementary Fig. 4a). Model mw30 (weak mantle width = 30 km) exhibits transient exhumation channel activity, moderate mantle exposure, and dual

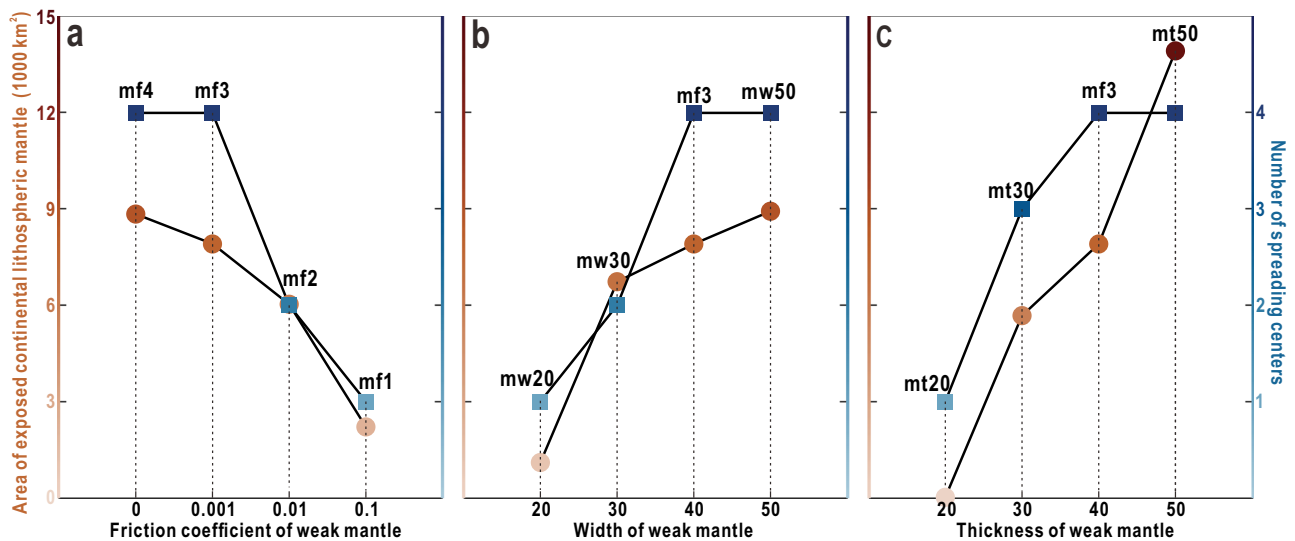


**Fig. 4 | Area of exposed lithospheric mantle and number of spreading centers affected by various physical parameters of the weak mantle. a** Various friction coefficients, **b** Various widths, **c** Various thicknesses. The squares refer to the number of spreading centers and that the circles refer to the area of exposed

continental lithospheric mantle. These graphs clearly show that the area of exhumed continental lithospheric mantle and the number of oceanic spreading centers increase for a lower friction coefficient, larger width or thickness of the weak mantle domain.

spreading centers (Fig. 4b; Supplementary Fig. 4b). Model mw50 (weak mantle width = 50 km) develops long-lived exhumation channels, promoting extensive mantle exposure and multiple spreading centers (Fig. 4b; Supplementary Fig. 4c).

Model mt20 (weak mantle thickness = 20 km) shows coupled crust-mantle rupture, negligible mantle exhumation, and a single stable spreading center (Fig. 4c; Supplementary Fig. 5a). Model mt30 (weak mantle thickness = 30 km) forms short-lived exhumation channels, moderate mantle exposure, and dual spreading centers with gradual abandonment of the older center (Fig. 4c; Supplementary Fig. 5b). Model mt50 (weak mantle thickness = 50 km, no gap between the weak mantle and the crust) preserves a large volume of weak mantle beneath continental margin, facilitating long-lived exhumation channels, extensive mantle exposure, and multiple spreading centers (Fig. 4c; Supplementary Fig. 5c).

In summary, our models show that a weak mantle zone with a smaller friction coefficient, larger width or thickness favors the formation of long-lived exhumation channels, thereby increasing the area of exhumed mantle lithosphere and the events of oceanic crust emplacement (Fig. 4).

Given that the rotational pole is located northeast of the Vavilov basin, the rifting rate in the northeast part of the basin is lower than the 4 cm/yr imposed in our reference model<sup>38</sup>. To investigate the effects of a slower extension velocity, we implemented a low-velocity model (mv3) with a rate of 3 cm/yr. In this model, the slower extension suppresses decompression melting, leading to decreased magmatic productivity. As a result, the COT developed only a single spreading center (Supplementary Fig. 6).

## Discussion

### Mantle exhumation punctuated with discrete oceanic crust in the Tyrrhenian basin

Our models show that lithospheric mantle is exhumed to the surface via exhumation channels that initiated within the weak mantle zone. Low-density, low-viscosity partially molten mantle flows towards these channels, resulting in exhumed mantle punctuated with multiple discrete oceanic crust emplacements. Model results are consistent with natural observations in the Tyrrhenian Basin. The existence of a lithospheric mantle zone that has been weakened prior to extension is

supported by the pronounced shear-wave low-velocity anomaly (40–80 km) within the uppermost mantle surrounds the Vavilov subbasin, which spatially correlates well with the subduction-related volcanism<sup>38,39</sup> (Fig. 1b). Furthermore, the modeled exhumation channels (>20 km below surface and maintain stable polarity) correspond to the large-scale detachment faults (that constitute the upper part of the exhumation channel) documented in the Vavilov subbasin<sup>20,38,40</sup>. The discrete oceanic crust manifests topographically as seamounts due to its lower density compared to the surrounding mantle lithosphere. Our reference model (4 cm/yr) develops three distinct spreading centers (spacing approximately 20 to 40 km) within its COT (Fig. 3g), mirroring several spreading centers may develop during the opening of the Southwestern Tyrrhenian Basin with high rifting velocity<sup>20</sup> (Fig. 1). In contrast, the model with a lower extension velocity (3 cm/yr) produced a single spreading center within the COT (Supplementary Fig. 6), consistent with the single Gortani MOR-basaltic Ridge identified in the northeastern Vavilov Basin that likely experienced a slower extension rate (Fig. 1a). Weak hydrated (fertile) and dry normal (depleted) continental lithospheric mantle were exhumed along the channel, with some exposed directly at the surface. These results align with geological observations of exceptionally heterogeneous and, on average, mineralogically fertile mantle sampled from the Tyrrhenian Basin<sup>16,17,22,26</sup>. According to Prada et al.<sup>19</sup>, the magmatic products, in particular those emplaced soon after the mantle exhumation (i.e., Vavilov and Magnaghi intraplate volcanoes) were intruded along fracture zones or deep penetrating extensional faults. The magmatic features dip eastwards, likely related to the normal faults at the western edge of the Basin, also dip eastwards<sup>19</sup>. However, because our model does not account for diiking processes, the magmatic products intruded along the shear zones are not included in our model.

### Magma-poor rifting and spreading can develop under fast-extension

Numerical modeling shows that extension rate governs lithospheric deformation during rifting<sup>10,37</sup>. Slow extension promotes strain localization along large-offset detachment faults, enabling deep mantle exhumation via simple-shear deformation. In contrast, rapid extension typically leads to distributed pure-shear thinning, favoring crust and

mantle lithosphere rupture synchronously, inhibiting significant mantle exposure<sup>37</sup>. This latter scenario aligns with the southwestern domain of our models, which lacks a weak mantle zone and exhibits simultaneous crust-mantle rupture under fast extension (Fig. 2; Supplementary Fig. 2). However, our models demonstrate that a sufficiently weakened lithospheric mantle zone can fundamentally alter this paradigm. Such a zone enables the development of exhumation channels (and associated detachment faults) even under high extension rates, facilitating deep mantle exhumation. This mechanism produces depth-dependent extension, wherein mantle rupture is delayed relative to the crust, analogous to the role of a strong lower crust under slow extension<sup>35</sup>. This explains the mantle exhumation observed in the rapidly extended Vavilov subbasin (4–6 cm/yr)<sup>23,25</sup>. Our work thus proposes that a sufficiently weakened mantle zone can enable mantle exhumation even under rapid rifting. This challenges the traditional view that slow extension is necessary for magma-poor margins, underscoring the importance of tectonic and petrological inheritance.

Notably, our magmatic-thermomechanical models reveal a distinct process within magma-poor COT: mantle exhumation punctuated with short-lived spreading centers (discrete oceanic crust). This contrasts with the prevailing conceptual magma-poor models that lithospheric mantle exhumation typically precedes oceanic spreading<sup>1–3</sup>. The switches between the emplacement of mantle and crust occur because the zone of partially molten mantle is not stable. Instead, it flows toward the exhumation channels initiated within the weak mantle zone. As the exhumation channel continues to be active, the partially molten mantle keeps migrating. This migration leads to the formation of multiple discrete spreading centers, with oceanic crust independently being emplaced atop each center. Given that the continental marginal basins are typically influenced by the dehydration of subducting slabs and may also develop a weak mantle zone<sup>27</sup>. We believe that the process of mantle exhumation being punctuated with emplacement of oceanic crust may be applicable to the other continental marginals (e.g., Banda Sea Basin, Okinawa Trough, Bransfield Basin). Similar to the Tyrrhenian Sea, the basement composition in these basins is marked by exhumed continental mantle, magmatic intrusions, and reorganized spreading systems<sup>27</sup>, which aligns with the processes in our models. However, due to the limited availability of ultra-deepwater drilling data and the scarcity of high-resolution geophysical profiles, this phenomenon may not have been fully recognized yet.

### Spreading centers jump towards the trench

Trench-ward jumps of spreading centers is a common process in marginal back-arc basins<sup>27,42</sup>. Multiple geodynamic mechanisms have been proposed to explain this phenomenon, which can be grouped into slab-related processes and mantle/plate interaction processes based on their driving factors. Slab-related processes are driven by the dynamics of the subducting slab itself, including (1) episodic trench retreat (directly related to slab rollback)<sup>27</sup>, (2) slab rotation triggered by buoyant indenter collision (slab deformation induced by external forces)<sup>43</sup>, and (3) slab interaction with the mantle transition zone<sup>24</sup>; Mantle/plate interaction processes on the other hand involve interactions between the mantle, overriding plate, or other lithospheric components, such as (1) plume-driven mantle flow<sup>41</sup>, and (2) the unbalance between the strength of transform faults bounding the basins and the strength of the overriding plate in narrow subduction zones<sup>42</sup> (lithospheric strength contrast-driven).

The opening of the young Tyrrhenian Sea was accompanied by multiple southeastward spreading center jumps toward the trench<sup>19,20</sup>. Our research shed light on this process, which differs from the above categories in several aspects: (1) The exhumation channel initiated from the weak mantle zone acts as a high extensional strain rate zone. (2) The partially molten mantle (characterized by low density and viscosity) consistently flows toward the channel to fill the space

created by rapid extension. Concurrently, there was a successive formation of spreading centers atop of the molten mantle. (3) The old spreading centers are gradually abandoned as the partially molten mantle is diverted to the exhumation channel. This mechanism involves strain localization in weak mantle zones and subsequent mantle flow redistribution. The numerical models presented here thus shed light on understanding spreading center jumps in marginal back-arc settings.

## Methods

### Governing equations

We use the geodynamic code I3ELVIS, which employs finite difference and marker-in-cell methods with irregular staggered Eulerian grids<sup>44–46</sup> to solve the continuity and momentum equations for incompressible flow and the energy equation. The governing equations of conservation of mass, momentum and energy are:

$$\frac{\partial v_i}{\partial x_i} = 0 \quad (1)$$

$$\frac{\partial \sigma'_{ij}}{\partial x_j} - \frac{\partial P}{\partial x_i} + \rho g_i = 0 \quad (2)$$

$$\rho c_p \left( \frac{\partial T}{\partial t} + v_i \frac{\partial T}{\partial x_i} \right) = \frac{\partial}{\partial x_i} \left( k \frac{\partial T}{\partial x_i} \right) + H_r + H_s + H_a + H_L \quad (3)$$

where  $v_i$  is the velocity,  $\sigma'_{ij}$  is the deviatoric stress tensor,  $P$  is the pressure,  $\rho$  is the density,  $g_i$  is the gravity acceleration,  $c_p$  is the heat capacity,  $T$  is the temperature,  $k$  is the thermal conductivity,  $H_r$ ,  $H_a$ ,  $H_s$  and  $H_L$  are radiogenic, adiabatic, frictional, and latent heating source, respectively.

### Method setup

The scale of the computational domain is 584 km (x-dimension) × 808 km (y-dimension) × 270 km (z-dimension) (Fig. 2a). The whole domain is resolved by 293 × 405 × 117 Eulerian nodes with a resolution of 2 × 2 × 2.5 km<sup>3</sup>. More than 240 million Lagrangian markers are randomly distributed in the model domain to track the physical properties, such as viscosity, plastic strain, and temperature. Free-slip boundary conditions are applied at the back wall (y = 808 km), top wall (z = 0 km), and at both the left and right walls (x = 0 and 584 km). The volume of material flowing out of the front boundary (y = 0) is compensated by the volume of material influx through the lower boundary (z = 290 km).

The compositional fields are shown with colors in Fig. 2a. The initial material field consists of a weak 20-km-thick sticky air layer, which allows the crustal surface to approximate a free surface<sup>47</sup>. The lithosphere is divided into a 15-km-thick upper crust (wet quartzite rheology), a 15-km lower crust (Felsic granulite rheology), a 70-km-thick lithospheric mantle (dry olivine rheology), and an underlying 170-km-thick asthenospheric mantle (dry olivine rheology) (Fig. 2). The initial geotherm in the crust increases linearly from 0 °C at the surface to 500 °C at the Moho. The initial geotherm in the lithospheric mantle increases linearly from 500 °C at the Moho to 1320 °C at the bottom of the lithosphere (Fig. 2). We assume an adiabatic gradient of 0.5 °C/km for the subcontinental asthenospheric mantle. The visco-plastic thermo-mechanical parameters of each lithology are based on a list of laboratory experiments.

### Rheology

A visco-plastic rheology is applied in the entire model domain with different rheological parameters for compositionally distinct layers. The viscous deformation in our models mainly follows the flow laws of

the dislocation creep.

$$\eta_{\text{dist}} = \frac{1}{2} A^{\frac{1}{n}} (\dot{\epsilon}_{\text{II}})^{\frac{1-n}{n}} \exp\left(\frac{PV_a + E_a}{nRT}\right) \quad (4)$$

where  $\dot{\epsilon}_{\text{II}}$  is the second invariant of the strain rate tensor,  $R$  gas constant,  $A$  pre-exponential factor,  $E_a$  activation energy,  $V_a$  activation volume, and  $n$  creep exponent. These values are listed in Supplementary Table 1.

Brittle/plastic rheology is controlled by fracture-related strain weakening<sup>46</sup>. It is implemented by using a Drucker-Prager criterion:

$$\eta_{\text{plas}} = \frac{\sigma_{\text{yield}}}{2\dot{\epsilon}_{\text{II}}} \quad (5)$$

$$\sigma_{\text{yield}} = C_\gamma + \varphi(P - P_f) \quad (6)$$

Where  $\eta_{\text{plastic}}$  is the effective viscosity of plastic rheology.  $\sigma_{\text{yield}}$  is the yield stress (Pa).  $P$  is the dynamic pressure on solids (Pa),  $P_f$  is the hydrostatic fluid pressure,  $C_\gamma$  is the plate strength at  $P - P_f = 0$  (for both tensile and confined fracture) that depends on the plastic strain  $\gamma$ , defined by:

$$C_\gamma = C_0, \text{ when } \gamma \leq \gamma_0 \quad (7)$$

$$C_\gamma = C_0 + (\gamma - \gamma_0) \frac{C_1 - C_0}{\gamma_1 - \gamma_0}, \text{ when } \gamma_0 < \gamma \leq \gamma_1 \quad (8)$$

$$C_\gamma = C_1, \text{ when } \gamma > \gamma_1 \quad (9)$$

$C_0$  and  $C_1$  are the initial and final strength values for the fracture-related weakening, respectively.  $\gamma_0$  and  $\gamma_1$  are the upper and lower strain limits for the fracture-related weakening, respectively.  $\varphi$  is the internal friction coefficient, defined by:

$$\left. \begin{aligned} \varphi &= \varphi_0, \text{ for } \gamma \leq \gamma_0 \\ \varphi &= \varphi_0 + (\gamma - \gamma_0) \frac{\varphi_1 - \varphi_0}{\gamma_1 - \gamma_0}, \text{ for } \gamma_0 < \gamma \leq \gamma_1 \\ \varphi &= \varphi_1, \text{ for } \gamma > \gamma_1 \end{aligned} \right\}, \text{ when } P \geq P_f (\text{confined fracture}) \quad (10)$$

$\varphi_0$  and  $\varphi_1$  are the upper and lower limits, respectively. Strain weakening is obtained by strain-dependent linear interpolation between parameterized minimum and maximum values of  $\varphi$  and  $C_\gamma$ .

Integrated plastic strain  $\gamma$  ( $t$  is time and  $\dot{\epsilon}_{ij(\text{plastic})}$  is the plastic strain rate tensor):

$$\gamma = \int \sqrt{\frac{1}{2} (\dot{\epsilon}_{ij(\text{plastic})})^2} dt \quad (11)$$

The effective viscosity is defined as the minimum value between the brittle/plastic and ductile viscosities, with further limitations imposed by the cut-off values. In the case of partially molten materials (such as partially molten mantle and crustal rocks), Gerya (2013)<sup>46</sup> investigated the effects of constant viscosities and the dry olivine flow law on the resulting spreading patterns. In light of the aforementioned results, a constant viscosity of  $10^{18}$  Pa-s (i.e., the lower cut-off viscosity) of the partially molten materials has been incorporated into the model.

## Magmatism

In order to model plate break-up and oceanic spreading, magma-related processes (melt generation, extraction, percolation and accretion) are implemented in our models in a simplified instantaneous process as described by Gerya (2013)<sup>46</sup>. The melt differentiation

and interaction of the melts and the mantle are not included. The melt fraction ( $M$ ) of the mantle is based on the parameterized melting model from Katz et al.<sup>48</sup>:

$$M = \begin{cases} 0 & \text{for } T \leq T_s \\ \frac{T - T_s}{T_l - T_s} & \text{for } T_s < T < T_l \\ 1 & \text{for } T \geq T_l \end{cases} \quad (12)$$

Where  $T_s$ ,  $T_l$  are the mantle solidus, mantle liquidus, respectively.

Partial melting occurs in a wide area similar to the melt pooling region<sup>49</sup>, and melt is extracted and stored in the shallowest part of the partial melting area. Lagrangian markers track the amount of melt extracted during model evolution. At each time step, a certain amount of melt is extracted based on the following formulation:

$$\delta M = M - \sum_{i=1}^n M_i^{\text{ext}} \quad (13)$$

where  $n$  is the previous extraction episodes, and  $M_i^{\text{ext}}$  is the extracted melt at each time step. The rock is considered non-molten when the extracted melt fraction is larger than the standard melt fraction ( $\delta M < 0$ ). Extracted mantle melts first travel vertically until they reach the mantle solidus surface under the lithosphere and then migrate along this surface toward regions with the highest local surface topography, where they form a crustal magma chamber. To ensure melt volume conservation and account for mantle compaction and subsidence in response to the melt extraction, melt addition to the bottom of the magma region is performed at every time step by converting shallowest markers of hot partially molten mantle into magma markers. At each time step, the volume of converted markers matches that of the extracted assembled melts computed for the time step. As a result of this treatment, the partially molten mantle always contains a small amount (<1 vol.%) of melt as this melt is continuously extracted and added to crustal magma chambers. The extracted melt at the next time step will be added to the bottom of the magma chamber.

Spontaneous cooling and crystallization of melts are implemented at the walls of the lower-crustal magma chambers by simply converting the rock type from molten to solid. This simple process does not account for volcanic and diking processes above the magma regions, so the magmatic products intruded along the shear zones are not included in our model.

## Data availability

The modeling data generated in this study have been deposited in the Zenodo repository (<https://doi.org/10.5281/zenodo.17627323>).

## Code availability

No new code has been developed for this study. The I3ELVIS code can be accessed at <https://zenodo.org/records/11486349>.

## References

- Boillot, G. et al. Ocean-continent boundary off the Iberian margin: A serpentinite diapir west of the Galicia Bank. *Earth Planet. Sci. Lett.* **48**, 23–34 (1980).
- Boillot, G. & Winterer, E. L. Drilling on the Galicia Margin: Retrospect and Prospect. *Proc. Ocean Drill. Proj. Sci. Results* **103**, 809–828 (1988).
- Whitmarsh, R. B., Manatschal, G. & Minshull, T. A. Evolution of magma-poor continental margins from rifting to seafloor spreading. *Nature* **413**, 150–154 (2001).
- Hauptert, I., Manatschal, G., Decarlis, A. & Unternehr, P. Upper-plate magma-poor rifted margins: Stratigraphic architecture and structural evolution. *Mar. Pet. Geol.* **69**, 241–261 (2016).
- Pérez-Gussinyé, M. et al. Towards a process-based understanding of rifted continental margins. *Nat. Rev. Earth Env.* **4**, 166–184 (2023).

6. Goodliffe, A. & Taylor, B. The boundary between continental rifting and sea-floor spreading in the Woodlark Basin, Papua New Guinea. *Geol. Soc. Spec. Publ.* **282**, 217–238 (2007).
7. Larsen, H. C. et al. Rapid transition from continental breakup to igneous oceanic crust in the South China Sea. *Nat. Geosci.* **11**, 782–789 (2018).
8. Tugend, J. et al. Reappraisal of the magma-rich versus magma-poor rifted margin archetypes. *Geol. Soc. Spec. Publ.* **476**, 23–47 (2018).
9. Zitellini, N., Malinverno, A. & Estes, E. R. International Ocean discovery program. Expedition 402 Scientific Prospectus: Tyrrhenian Continent–Ocean Transition. <https://doi.org/10.14379/iodp.sp.402.2023> (2023).
10. Pérez-Gussinyé, M., Morgan, J. P., Reston, T. J. & Ranero, C. R. The rift to drift transition at non-volcanic margins: Insights from numerical modelling. *Earth Planet. Sci. Lett.* **244**, 458–473 (2006).
11. Ros, E. et al. Lower Crustal Strength Controls on Melting and Serpentinization at Magma-Poor Margins: Potential Implications for the South Atlantic. *Geochem. Geophys. Geosyst.* **18**, 4538–4557 (2017).
12. Michael, P. J. et al. Magmatic and amagmatic seafloor generation at the ultraslow-spreading Gakkal ridge, Arctic Ocean. *Nature* **423**, 956–961 (2003).
13. Kastens, K. & Mascle, J. The Geological Evolution of the Tyrrhenian Sea: An Introduction to the Scientific Results of ODP Leg 107. *Proc. Ocean Drill. Prog. Sci. Res.* **107**, 3–26 (1990).
14. Sartori, R. The Main Results of ODP Leg 107 in the Frame of Neogene to Recent Geology of Perityrrhenian Areas. *Proc. Ocean Drill. Prog. Sci. Res.* **107**, 715–730 (1990).
15. Sartori, R. et al. Crustal features along a W–E Tyrrhenian transect from Sardinia to Campania margins (Central Mediterranean). *Tectonophysics* **383**, 171–192 (2004).
16. Bonatti, E., Seyler, M., Channell, J., Giraudeau, J. & Mascle, G. Peridotites drilled from the Tyrrhenian Sea, ODP Leg 107. *Proc. Ocean Drill. Prog. Sci. Res.* **107**, 37–47 (1990).
17. Beccaluva, L. Geochemistry and mineralogy of volcanic rocks from ODP Sites 650, 651, 655, and 654 in the Tyrrhenian Sea. *Proc. Ocean Drill. Prog. Sci. Res.* **107**, 49–74 (1990). (1990).
18. Greve, S., Paulssen, H., Goes, S. & van Bergen, M. Shear-velocity structure of the Tyrrhenian Sea: Tectonics, volcanism and mantle (de)hydration of a back-arc basin. *Earth Planet. Sci. Lett.* **400**, 45–53 (2014).
19. Prada, M. et al. Seismic structure of the Central Tyrrhenian basin: Geophysical constraints on the nature of the main crustal domains. *J. Geophys. Res. Solid Earth* **119**, 52–70 (2014).
20. Prada, M., Ranero, C. R., Sallarès, V., Zitellini, N. & Grevemeyer, I. Mantle exhumation and sequence of magmatic events in the Magnaghi–Vavilov Basin (Central Tyrrhenian, Italy): New constraints from geological and geophysical observations. *Tectonophysics* **689**, 133–142 (2016).
21. Prada, M. et al. The structure of Mediterranean arcs: New insights from the Calabrian Arc subduction system. *Earth Planet. Sci. Lett.* **548**, 116480 (2020).
22. Zitellini, N. et al. Recent inversion of the Tyrrhenian Basin. *Geology* **48**, 123–127 (2020).
23. Faccenna, C., Becker, T., Lucente, F., Jolivet, L. & Rossetti, F. History of subduction and back-arc extension in the Central Mediterranean. *Geophys. J. Int.* **145**, 809–820 (2001).
24. Faccenna, C., Funiciello, F., Giardini, D. & Lucente, P. Episodic back-arc extension during restricted mantle convection in the Central Mediterranean. *Earth Planet. Sci. Lett.* **187**, 105–116 (2001).
25. Guillaume, B., Funiciello, F., Faccenna, C., Martinod, J. & Olivetti, V. Spreading pulses of the Tyrrhenian Sea during the narrowing of the Calabrian slab. *Geology* **38**, 819–822 (2010).
26. Sanfilippo, A. et al. Heterogeneous Earth’s mantle drilled at an embryonic ocean. *Nat. Commun.* **16**, 2016 (2025).
27. Magni, V., Naliboff, J., Prada, M. & Gaina, C. Ridge Jumps and Mantle Exhumation in Back-Arc Basins. *Geosci* **11**, 475 (2021).
28. Magrini, F. et al. Surface-Wave Tomography of the Central-Western Mediterranean: New Insights into the Liguro-Provençal and Tyrrhenian Basins. *J. Geophys. Res. Solid Earth* **127**, e2021JB023267 (2022).
29. Ranalli, G. & Murphy, D. C. Rheological stratification of the lithosphere. *Tectonophysics* **132**, 281–295 (1987).
30. Hilaret, N. et al. High-Pressure Creep of Serpentine, Interseismic Deformation, and Initiation of Subduction. *Science* **318**, 1910–1913 (2007).
31. Buck, R. Modes of Continental Lithospheric Extension. *J. Geophys. Res.* **962**, 20161–20178 (1991).
32. le pourhiet, L., Burov, E. & Moretti, I. Rifting through a stack of inhomogeneous thrusts (the dipping pie concept). *Tectonics* **23**, TC4005 (2004).
33. Brune, S., Heine, C., Perez-Gussinye, M. & Sobolev, S. V. Rift migration explains continental margin asymmetry and crustal hyper-extension. *Nat. Commun.* **5**, 4014 (2014).
34. Brune, S., Heine, C., Clift, P. D. & Pérez-Gussinyé, M. Rifted margin architecture and crustal rheology: Reviewing Iberia-Newfoundland, Central South Atlantic, and South China Sea. *Mar. Pet. Geol.* **79**, 257–281 (2017).
35. Huisman, R. & Beaumont, C. Depth-dependent extension, two-stage breakup and cratonic underplating at rifted margins. *Nature* **473**, 74–78 (2011).
36. Lavier, L. L. & Manatschal, G. A mechanism to thin the continental lithosphere at magma-poor margins. *Nature* **440**, 324–328 (2006).
37. Huisman, R. & Beaumont, C. Roles of lithospheric strain softening and heterogeneity in determining the geometry of rifts and continental margins, in Imaging, Mapping and Modelling Continental Lithosphere Extension and Breakup. *Geol. Soc. Spec. Publ.* **282**, 111–138 (2007).
38. Milia, A., Torrente, M. M. & Tesauro, M. From stretching to mantle exhumation in a triangular backarc basin (Vavilov basin, Tyrrhenian Sea, Western Mediterranean). *Tectonophysics* **710–711**, 108–126 (2017).
39. Marfo, D., Aoudia, A., Pachhai, S. & Kherchouche, R. 3D shear wave velocity model of the crust and uppermost mantle beneath the Tyrrhenian basin and margins. *Sci. Rep.* **9**, 1–10 (2019).
40. Loreto, M. F., Zitellini, N., Ranero, C. R., Palmiotto, C. & Prada, M. Extensional tectonics during the Tyrrhenian back-arc basin formation and a new morpho-tectonic map. *Basin Res* **33**, 138–158 (2021).
41. Ito, G., Lin, J. & Graham, D. Observational and theoretical studies of the dynamics of mantle plume–mid-ocean ridge interaction. *Rev. Geophys.* **41**, 1017 (2003).
42. Schliffke, N., van Hunen, J., Allen, M. B., Magni, V. & Gueydan, F. Episodic back-arc spreading centre jumps controlled by transform fault to overriding plate strength ratio. *Nat. Commun.* **13**, 582 (2022).
43. Wallace, L. M., Ellis, S. & Mann, P. Collisional model for rapid fore-arc block rotations, arc curvature, and episodic back-arc rifting in subduction settings. *Geochem. Geophys. Geosyst.* **10**, Q05001 (2009).
44. Gerya, T. V. & Yuen, D. A. Characteristics-based marker-in-cell method with conservative finite-differences schemes for modeling geological flows with strongly variable transport properties. *Phys. Earth Planet. Inter.* **140**, 293–318 (2003).
45. Gerya, T. V. & Yuen, D. A. Robust characteristics method for modelling multiphase visco-elasto-plastic thermo-mechanical problems. *Phys. Earth Planet. Inter.* **163**, 83–105 (2007).
46. Gerya, T. V. Three-dimensional thermomechanical modeling of oceanic spreading initiation and evolution. *Phys. Earth Planet. Inter.* **214**, 35–52 (2013).

47. Cramer, F. et al. A comparison of numerical surface topography calculations in geodynamic modelling: An evaluation of the 'sticky air' method. *Geophys. J. Int.* **189**, 38–54 (2012).
48. Katz, R. F., Spiegelman, M. & Langmuir, C. H. A new parameterization of hydrous mantle melting. *Geochem. Geophys. Geosyst.* **4**, 1073 (2003).
49. Gregg, P. M., Behn, M. D., Lin, J. & Grove, T. L. Melt generation, crystallization, and extraction beneath segmented oceanic transform faults. *J. Geophys. Res. Solid Earth* **114**, 1–16 (2009).

## Acknowledgements

W.L. acknowledges funding from the National Natural Science Foundation of China (Grant no.: 42425402). J.L. acknowledges funding from the National Natural Science Foundation of China (Grant no.: 42222406). H.S. is partially supported by the Natural Science Foundation of China (42274066). S.B. has been funded by the European Union (ERC, EMERGE, 101087245). Numerical simulations were run on the supercomputing system in the Supercomputing Center of the University of Science and Technology of China and the clusters of the National Supercomputer Center in Guangzhou (Tianhe-II).

## Author contributions

H.S., W.L., and J.L. conceived the initial idea and model. H.S. performed numerical experiments. H.S., W.L., J.L., and S.B. participated in result interpretation and paper preparation.

## Competing interests

The authors declare no competing interests.

## Additional information

**Supplementary information** The online version contains supplementary material available at <https://doi.org/10.1038/s41467-025-68052-1>.

**Correspondence** and requests for materials should be addressed to Wei Leng or Jie Liao.

**Peer review information** *Nature Communications* thanks Manel Prada, Nevena Andrić-Tomašević, and the other anonymous reviewer(s) for their contribution to the peer review of this work. A peer review file is available.

**Reprints and permissions information** is available at <http://www.nature.com/reprints>

**Publisher's note** Springer Nature remains neutral with regard to jurisdictional claims in published maps and institutional affiliations.

**Open Access** This article is licensed under a Creative Commons Attribution-NonCommercial-NoDerivatives 4.0 International License, which permits any non-commercial use, sharing, distribution and reproduction in any medium or format, as long as you give appropriate credit to the original author(s) and the source, provide a link to the Creative Commons licence, and indicate if you modified the licensed material. You do not have permission under this licence to share adapted material derived from this article or parts of it. The images or other third party material in this article are included in the article's Creative Commons licence, unless indicated otherwise in a credit line to the material. If material is not included in the article's Creative Commons licence and your intended use is not permitted by statutory regulation or exceeds the permitted use, you will need to obtain permission directly from the copyright holder. To view a copy of this licence, visit <http://creativecommons.org/licenses/by-nc-nd/4.0/>.

© The Author(s) 2026